New Insight into Hierarchical Structures of Carbon Black Dispersed in Polymer Matrices: A Combined Small-Angle Scattering Study

Tadanori Koga,*,†,‡ Takeji Hashimoto,*,†,§,|| Mikihito Takenaka,†,§ Kazuya Aizawa,# Naoya Amino,○ Masao Nakamura,†,◇ Daisuke Yamaguchi,|| and Satoshi Koizumi||

Hashimoto Polymer Phasing Project, ERATO, JST, Japan, Chemical and Molecular Engineering Program, Department of Materials Science and Engineering, Stony Brook University, Stony Brook, New York 11794-2275, Department of Polymer Chemistry, Graduate School of Engineering, Kyoto University, Katsura, Nishikyo-ku, Kyoto 661-8510, Japan, Advanced Science Research Center and Quantum Beam Science Directorate, Japan Atomic Energy Agency, Tokai, Ibaraki 319-1195, Japan, The Yokohama-rubber Company, Ltd., 2-1 Oiwaki, Hiratsuka, Kanagawa, 254-8601, Japan, and ZEON Corporation, 1-2-1, Yako, Kawasaki, Kanagawa, 210-8507, Japan

Received August 17, 2007; Revised Manuscript Received November 7, 2007

ABSTRACT: Using a combined ultra-small-angle and small-angle scattering (CSAS) method of neutrons and X-rays, we investigated hierarchical structures of carbon black (CB) highly loaded in polyisoprene (PI) and poly(styrene-*random*-butadiene) copolymer (SBR) under mechanical field (defined respectively as CB/PI and CB/SBR) as well as in toluene under a sonic field (defined as CB/toluene). In order to analyze each structure level comprising the hierarchical structures of CB from the CSAS profiles, we employed the unified Guinier/power-law approach proposed by Beaucage (*J. Appl. Cryst.* **1995**, *28*, 717). Furthermore, in order to extract not only sizes but also shapes of the structure elements, we developed a modified approach, in which the Guinier scattering function utilized in the Beaucage approach was replaced by a form factor of the corresponding structure. Comparison of the scattering profiles from CB/PI and CB/SBR with CB/toluene clarified that (i) the smallest structure elements of CB (that further form mass-fractal objects) in PI and SBR were not an unbreakable unit of the CB filler which resulted after sonification in toluene but were instead composed of the several unbreakable units bounded together by polymer chains (defined as "dispersible units") and (ii) sizes and shapes of the dispersible units depended on the polymer matrix: Its size was larger in PI than in SBR. (iii) Moreover, the enlarged size of the dispersible unit in PI was found to enlarge the upper cutoff length of the mass-fractal structure in PI, while the mass-fractal dimensions themselves remained unchanged between PI and SBR. Hence, the detailed characterizations of the hierarchical structures by using CSAS shed new light on the dispersion process of the filler compound in the polymer matrix.

I. Introduction

It is believed to be a fundamental question not only in macromolecular science but also in physical science, in general, to explore basic principles in order to attain controlled spatial arrangements of metal, inorganic, and organic particles in a polymer matrix or to develop methodologies for characterizing their structures and responses to external stimuli. As a model system for a study along this line, in this study, we focus on a carbon black (CB) filler in rubber (CB/rubber), which is well-known as one of the most successful nanocomposites for industry.[1] We wish to obtain a new insight into the historically and traditionally long-standing studies of the structure by using a modern methodology of a combined small-angle scattering (CSAS) method, as will be detailed below. By using the CSAS method, we aim to collect, in situ, statistically averaged information over a large sample area in order to elucidate systematically three-dimensional (3d) spatial arrangements of the filler particles over a wide length scale ranging from a few nanometers to a few tens of micrometers for given CB/rubber systems. Although the works to be reported here are concerned only with a static structure analysis of as-compounded CB/rubber systems, we hope to eventually clarify the mechanism of the structure formation for CB fillers in the complex CB/rubber systems. Furthermore, we anticipate that we can treat the complex systems on the basis of fundamental physical science in soft matter.

An important aspect of the reinforcement of rubberlike polymers is how to properly disperse filler particles in rubber matrices during conventional compounding processes of rubbers and fillers. It is well-known that CB primary particles are fused together into "aggregates" that are the characteristic units of CB and considered unbreakable under further dispersion processes of CB in rubber[2] (see Figures 12 and 13 to be discussed later). Real rubber compounds always have higher order structures composed of the aggregates, called as "agglomerates". The presence of the agglomerates is generally considered to strongly affect reinforcing properties of rubbers.[2] Different combinations of rubbers and fillers show different behavior in compounding processes, which in turn is expected to create a variety of agglomerates and to result in varying physical properties of rubber compounds. At present, however, the relationships among the compounding conditions, agglomerates, and reinforced properties have not been fully understood on a scientific base. They have been rather understood on an empirical "know-how" base.[3] In order to understand the

* To whom correspondence should be addressed. E-mail: tkoga@notes.cc.sunysb.edu (T. K.); hashimoto.takeji@jaea.go.jp (T. H.)
† Hashimoto Polymer Phasing Project, ERATO, JST.
‡ Chemical and Molecular Engineering Program, Department of Materials Science and Engineering, Stony Brook University.
§ Department of Polymer Chemistry, Graduate School of Engineering, Kyoto University.
|| Advanced Science Research Center, Japan Atomic Energy Agency.
Quantum Beam Science Directorate, Japan Atomic Energy Agency.
○ The Yokohama-rubber Co., Ltd.
◇ ZEON Co.

10.1021/ma071867l CCC: $40.75
Published on Web 12/21/2007

relationships, it is especially crucial to quantitatively investigate structural responses of filler particles against mechanical stimuli over a wide length scale. As a first step of this investigation, we believe it is important to develop a basic methodology, with which *statically averaged information* of the structures of the filler particles in space can be *quantitatively characterized in situ* over a sufficiently large sample area.

Our objective in this study is to explore the hierarchical structures of the CB filler in rubbers with a filler content that is typically needed for commercial applications such as rubber tires and tire-forming bladders. Conventional transmission electron microscopy (TEM) has been extensively used so far to investigate the filler structures.[4−8] Great interests are currently being focused on an electron tomography (ET)-TEM technique for analyzing 3d spatial distributions of fillers in rubbers.[9] However, high concentrations of filler particles loaded in rubbers will make a TEM image analysis difficult, primarily because of an overlapping of the structures along the electron beam axis. Furthermore, the TEM analysis requires ultrathin-sectioning of specimens into 50−100 nm thickness so that detailed characterizations of 3d organization of the filler in a rubber matrix may not be easily attained, when the size of the 3d structures exceeds the thickness of ultrathin sections. This is also the case even when the sophisticated ET-TEM method is applied to the systems.[9]

In order to overcome these difficulties discussed above, the approach that we are focusing on is small-angle scattering (SAS) techniques which can provide us morphological features over several orders in length scales (∼nm to ∼μm) under various environments. So far, ultra-small-angle scattering (USAS)[10] and conventional small-angle scattering (SAS) techniques using various radiations, such as X-ray,[11−18] neutron,[10,14,19,20] and light,[21,22] have been utilized to explore the hierarchical structures of CB or silica (Si) fillers reinforced rubbers. However, the hierarchical structures of these fillers highly loaded in rubbers have not yet been studied systematically and extensively by using these various scattering methods in concert, albeit elucidation and manipulation of the morphology could be a key for controlling macroscopic properties of rubber-reinforced compounds. Here we choose the following USAS and SAS to achieve the goal. (i) Bonse−Hart type ultra-small-angle neutron scattering (USANS)[23] that can reach the smallest q value[24] of 3.0×10^{-4} nm^{-1}, where q is the magnitude of the scattering vector defined by $q = (4\pi/\lambda)\sin(\theta/2)$ with λ and θ being the wavelength of the incident beam and the scattering angle in the medium, respectively. Its spatial resolution is almost equivalent to that of a conventional laser light scattering (LS) technique, which cannot be applied easily to filler reinforced rubbers due to a turbidity−absorption problem. However, USANS overcomes more easily the difficulty of the turbidity−absorption problem than the LS method because of a relatively high transmittance of neutron beams with matters. (ii) In order to cover the higher q range ($q \geq 1 \times 10^{-2}$ nm^{-1}) inaccessible by USANS, the Bonse−Hart type ultra-small-angle X-ray scattering (USAXS) camera,[25] which covers the q range of $0.002 < q < 0.45$ nm^{-1}, and a conventional small-angle X-ray scattering (SAXS) camera, which covers the q range of $0.1 < q < 6$ nm^{-1}, are utilized in the laboratory. The combination of these three techniques allows us to measure scattering profiles over the length scales from 1 nm $< q^{-1} <$ 21 μm.

In this paper, we focus on the morphological characterizations of CB in two different polymer matrices, i.e., polyisoprene (PI) and poly(styrene-*random*-butadiene) copolymer (SBR) with the same loading of CB (volume fraction of 20%). In order to analyze each structure level comprising the hierarchical structures, we first utilized the so-called unified approach proposed by Beaucage who approximated scattering data as the Guinier scattering function combined with a structurally limited power-law scattering.[26] In this approach the power-law scattering serves to express 3d organization of the elemental structural unit, while the size of the elemental structural unit itself is described by the Guinier scattering function. However, the shape of the structural unit remains unresolved in the context of the unified approach. In order to extract information on the shape of the structural unit, we propose a modified unified analysis in which the Guinier function is replaced by a form factor of the corresponding structural unit. A combined use of these approaches can provide us a deep insight into the hierarchical structures of CB dispersed in rubbers under a mechanical field as well as in toluene under a sonic field. The detailed characterizations of the hierarchical structure would be crucial in understanding of rubber reinforcement as well as development of new and improved types of filler particles for specific applications.

Table 1. Characterizations of Polymers Used in This Study

polymers	M_w	M_w/M_n	w_{PS}(%)[a]	vinyl content (%)[b]
SBR	5.0×10^5	3.4	23.5	15
PI	1.2×10^6	2.7		

[a] Weight fraction of styrene content [b] Vinyl content in PB sequence

II. Experimental Methods

II-1. Sample Characterizations. The CB filler (SHOBLOCK N339, Showa Cabot, Chiba, Japan) was used in this study. The mean radius of the CB filler (R_{TEM}) was determined to be 13 nm from TEM. The density of the CB filler was 1.8 g/cm^3. The elastomers used in this study were PI (ZEON Co., Kawasaki, Japan) and SBR (ZEON Co.). Their material characteristics are listed in Table 1. The volume fraction of the CB filler was fixed to 20%, the high loading of which is typically required in commercial applications for enhancing mechanical properties of rubbers. Specific surface areas measured using nitrogen adsorption method and the dibuthyl phtalate absorption for the CB filler were determined to be 90 m^2/g and 1.18 mL/g, respectively. The CB filler was compounded into the rubbers by using a Banbury mixer, heated to $T = 80$ °C for 5 min. The CB/rubber compounds were then mixed with di-*tert*-butylperoxydiisopropylbenzene as a curing agent using an open roll mill. The un-cross-linked and cross-linked rubbers were subsequently pressed in a mold at $T = 100$ °C for 4 min and at 170 °C for 20 min, respectively.

II-2. USANS Measurements. Our USANS measurements were conducted with the PNO spectrometer installed at the beamline of the JRR-3 research reactor at JAEA, Tokai, Japan. The details of the USANS setup have been described elsewhere.[24] Two single-bounce silicon (111) single crystals were used; one is to monochromatize and collimate the incident beam, and the other is to analyze the scattered beam. The neutron wavelength was set to 0.2 nm. As shown in Figure 1, the strong excess scattering intensity from the CB filler was observed relative to the background scattering from the empty cell in the entire q range between $q_{min} \approx 3.0 \times 10^{-4}$ nm^{-1} and $q_{max} \approx 1 \times 10^{-2}$ nm^{-1}. Hence this q range was used for this study.

II-3. USAXS Measurements. The details of our lab-based USAXS camera have been described elsewhere.[25] Four-bounced (220) Bragg reflections from germanium channel-cut crystals (the Bragg angle is 22.65° with Cu Kα_1 radiation) were used in both monochromator and analyzer. In addition, owing to an asymmetric Bragg reflection mixed in the rigid monochromator, the incident beam flux can be increased by a factor of 4, compared to that without the installation.[25,27] With our USAX*S* configuration, the q range of 0.002 to 0.45 nm^{-1}, which is partially overlapped with those of USANS and SAXS results, could be covered. Thus, the

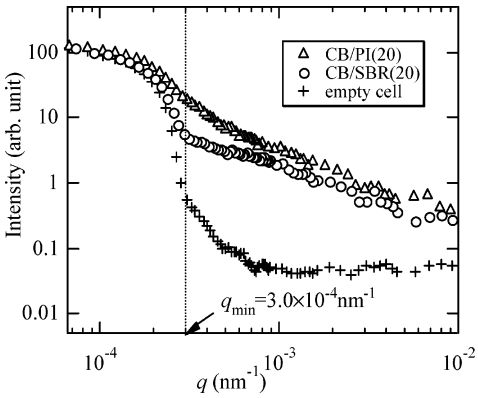

Figure 1. USANS rocking curves obtained with samples of CB/PI-(20) (triangles), CB/SBR(20) (circles), and with a empty cell (crosses). All the curves were corrected for absorption.

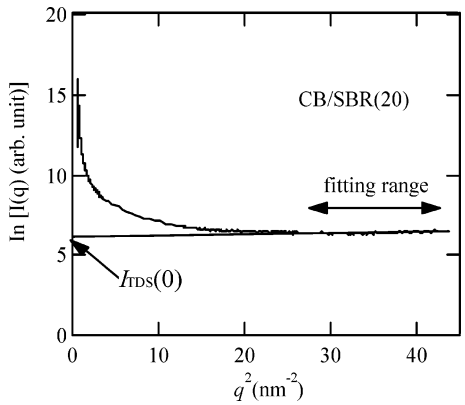

Figure 2. Natural logarithm of SAXS intensity $I(q)$ vs q^2 for CB/SBR(20).

use of USAXS overcomes the demerit caused by the high-intensity background in the large-q tail of the USANS rocking curve and by the low-q resolution limit of SAXS.

II-4. SAXS Measurements. SAXS profiles were taken with an apparatus that consists of an 18 kW rotating-anode X-ray generator with a copper target (M18XHF-SRA, MAC Science Co., Ltd., Yokohama, Japan, now Bruker AXS K.K., Yokohama, Japan), a graphite monochromator, a 2.0 m camera from the sample to the detector, and a one-dimensional position sensitive proportional counter (PSPC). The exposure time for each measurement was set to 30 min. It is important to take the contribution of thermal diffuse scattering (TDS) into account for scattering profiles at the higher q-region. TDS is known to be caused by acoustic phonons propagating in a media. The scattering intensity of TDS, $I_{TDS}(q)$, is approximated by[28]

$$I_{TDS}(q) = I_{TDS}(0)\exp(cq^2) \quad (1)$$

where c is a constant and $I_{TDS}(0)$ is an extrapolated scattering intensity at $q = 0$. The $I_{TDS}(0)$ values were estimated from the best-fit between eq 1 and the experimental data in the q-region at $28 < q^2 < 43$ nm^{-2} where ln I vs q^2 plots show a linear relationship, as shown in Figure 2.

Film thickness of each sample was optimized for the X-ray scattering measurements, i.e., $\mu t = 1$, where μ is the linear absorption coefficient of X-ray for the system to be studied and t is the film thickness. All the samples were measured at room temperature under atmospheric pressure. USANS, USAXS, and SAXS scattering profiles were corrected for the air scattering, absorption, and the slit-width and slit-height smearings. X-ray scattering data were measured on an absolute intensity scale by using the nickel-foil method,[29] and the neutron data were then shifted vertically to make them match with X-ray scattering data with an overlap q range in the logarithmic intensity scale. The

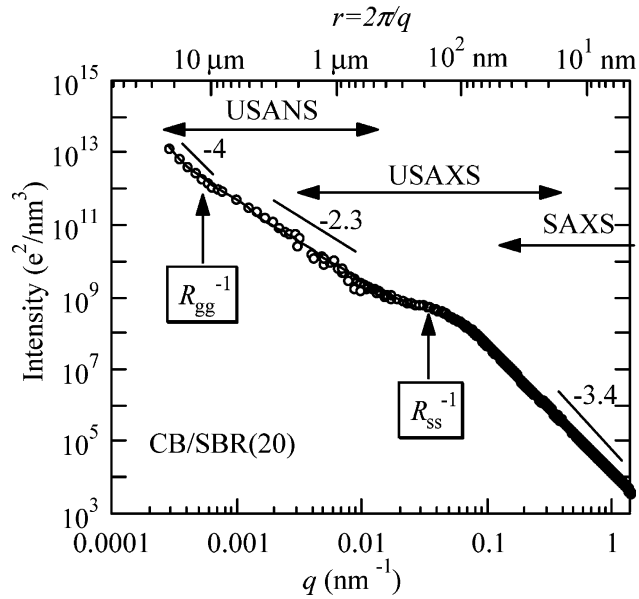

Figure 3. Combined USANS, USAXS, and SAXS profiles for CB/SBR(20) (open circles) in the absolute intensity scale of X-ray scattering. The two arrows marked by R_{gg}^{-1} and R_{ss}^{-1} indicate an existence of Guinier scattering having radii of gyration R_{gg} and R_{ss} which also indicate the upper and lower cutoff lengths for the mass-fractal structure. The solid line is the best-fitted theoretical scattering profile obtained from eq 5.

vertical shift of the neutron scattering data in the logarithmic scale corresponds to a conversion of the absolute scattering intensity scale of the neutron scattering data to that of the X-ray scattering data for a given system (CB particles dispersed in the rubber matrix) of our interest, the basic principles of which has been presented elsewhere.[30] Therefore, we specify the absolute intensity scale of the combined X-ray and neutron scattering intensity profile shown in Figures 3, 5, and 8 with respect to that of the X-ray profile.

II-5. TEM Experiments. The films were microtomed at $T = -100$ °C, using a LEICA Ultracut UCT sectioning system (LEICA Microsystems K.K., Tokyo, Japan). The ultrathin sections without staining were measured with a transmission electron microscope at 200 kV (H-800, Hitachi, Tokyo, Japan).

III. Results

III-1. Remarks on Terminologies. Before moving into the main topics, it would be useful to describe the terminologies to be used. In this study, we characterized CB filler particles dispersed in toluene under a sonic field or those dispersed in rubbers under a mechanical field, as will be detailed later in this section. We found the following facts. (i) The smallest unbreakable unit of the CB filler resulted from sonification of the CB/toluene solution had a spherical shape and consisted of about nine primary CB particles fused together. (ii) The unbreakable unit was further clustered into a higher order structure in the rubber matrices. The unbreakable unit and the higher-order structure are called *aggregate* and *agglomerate*, respectively, in the context of the common terminology in this field. However, later in this section, we shall further clarify the agglomerate comprises two structure levels: "*dispersible unit*" (or *agglomerate level 1*) and "*mass-fractal structure*" (or *agglomerate level 2*). The dispersible unit (or agglomerate level 1) is *the smallest structural unit in the rubber matrix* which is composed of the *aggregates* and further forms a higher order structure defined as the mass-fractal structure (or agglomerate level 2). In this sense, the dispersible unit is equivalent to the "lower cutoff object" for the mass-fractal structure formed

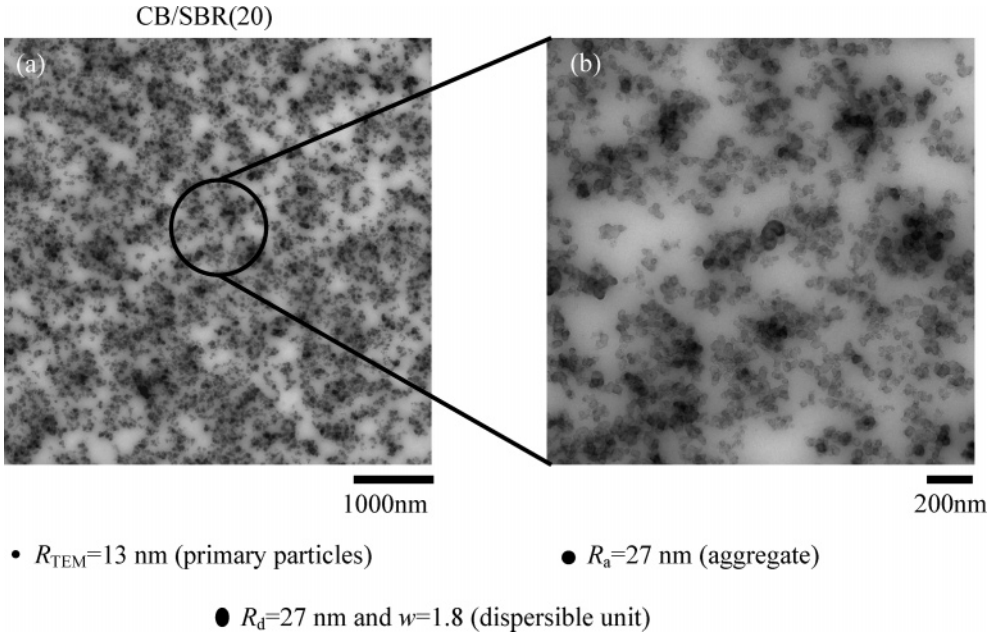

Figure 4. TEM image for CB/SBR(20) with a low magnification (part a) and a high magnification (part b).

in the rubbers. The hierarchical structures of CB in toluene and in the rubbers will be schematically summarized later in Figures 12 and 13. We believe that the distinction of the two kinds of the agglomerates, agglomerate level 1 and agglomerate level 2, as well as the distinction between the aggregate and dispersible unit, are essential for a better understanding of the hierarchical structures in the rubber matrix, as will be clarified in the text. Hereafter we define agglomerate level 1 as the "dispersible unit" and agglomerate level 2 as the "agglomerate", unless otherwise stated.

III-2. CB in SBR Matrix. Figure 3 shows the scattering profile for the peroxide cross-linked CB/SBR(20) obtained by a combined use of USANS, USAXS, and SAXS, which covers the wide q range of 3.0×10^{-4} to 1.5 nm^{-1} (length scale r from a few nanometers to a few 10 μm, about 4 orders of magnitude, as shown in the top abscissa). The intensity scale covered is also wide, about 10 orders of magnitude. From the figure, we can see three power-law scattering profiles given by

$$I(q) \sim q^{-p} \tag{2}$$

in the observed q range: At the high q range ($0.2 < q < 1.5$ nm^{-1}), the power-law behavior with $p = 3.40 \pm 0.04$ is seen, suggesting that surface of the primary particles is not smooth but rough characterized by surface fractal, as suggested by the earlier works[11,31] and as will be clarified later in section IV-1. If this is the case the surface fractal dimension (D_s) for CB/SBR(20) is estimated to be 2.6, because D_s is related to the power-law exponent p

$$p = 2d - D_s \tag{3}$$

where d is the Euclidean dimension of the space (in this case, $d = 3$). According to the previous small-angle neutron scattering (SANS) experiments,[32] the pure CB fillers had $p = 3.67$ at the high q-region regardless of the CB grade. This power is slightly larger than that of CB/SBR(20), but is in good agreement with our SAXS data for CB/toluene ($p = 3.6$), as will be shown later in Figure 6.

The power law with $p = 2.30 \pm 0.05$ is seen in the q range from 0.0012 to 0.012 nm^{-1}, indicating that the existence of mass-fractal structure with a mass fractal dimension (D_m) characterized by

$$p = D_m \tag{4}$$

Therefore, D_m is determined to be 2.3, which is almost equivalent to that in the pure CB powder ($D_m = 2.4$) obtained by a TEM analysis.[8] The apparent power law with $p = 4.0$ is seen at the very low q range of $0.0003 < q < 0.0005$ nm^{-1}. The term "apparent" is coined, because the power law is only seen over the very narrow q range due to a limitation of the low-q resolution of the USANS apparatus for this particular sample. The scattering in this q range is primary attributed to a large-q tail of the form factor of the agglomerate as a whole which contains the mass-fractal object as its internal structure, as will be discussed later.

Another important aspect in the scattering profile for CB/SBR(20) is the two discrete form-factor profiles which can be assumed by Gaussian functions (the Guinier scattering functions) as indicated by the arrows in Figure 3. The positions of the arrows correspond to R_{gg}^{-1} and R_{ss}^{-1}, where R_{gg} and R_{ss}, respectively, correspond to the upper and lower cutoff lengths of the mass fractal structure, as will be clarified in section IV-1 later. In the next section, using the unified equation and its modification, we will separate the contribution of the scattering intensity from each structure level comprising the hierarchical structures.

It is important to note that (i) the power law of $q^{-3.4}$ is observed to persist at $q \geq 0.2$ nm^{-1}, implying that the lower cutoff wave number for the surface fractal object is about 0.2 nm^{-1} (as will be clarified later in conjunction with Figure 8) and (ii) this value is much larger than the lower cutoff wave number $R_{ss}^{-1} = 0.03$ nm^{-1} for the mass fractal object. The relationship between points i and ii reveals that the self-similar surface roughness exists on the surface of the lower cutoff object having the characteristic length R_{ss}.

Figure 4 shows a representative TEM image for CB/SBR-(20) at a low magnification (part a) and a high magnification (part b). In the figure legends, we added the corresponding size of each structure element obtained from the scattering results to be discussed later. We recognized that no isolated primary

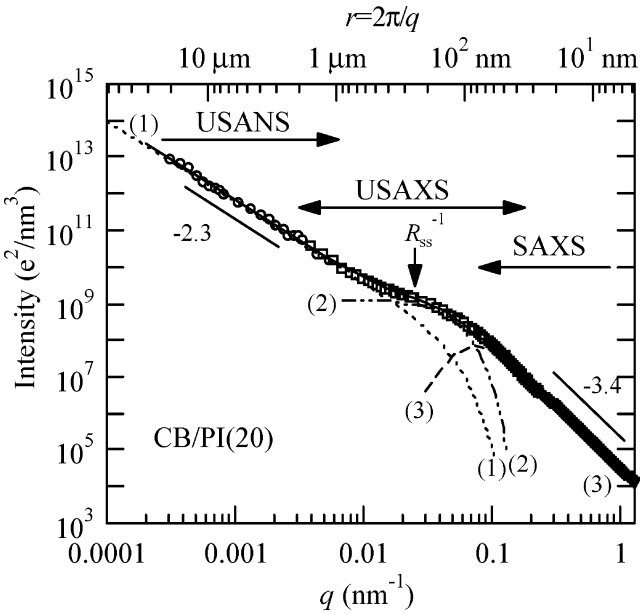

Figure 5. Combined USANS, USAXS, and SAXS profiles for CB/PI(20) (symbols). The solid line is the best-fitted theoretical profile obtained from eq 6. The dotted lines numbered 1 to 3 are the contribution of the first to the third term in the rhs of eq 6 to the net theoretical scattering profile.

particles were apparently found in the rubber matrix. Instead, the CB primary particles appear to be mutually fused to form their higher order structures, i.e., the aggregate, or the dispersible unit (agglomerate 1). However, as expected, it turned out that the detailed characterizations of their 3d morphology were very complicated because of the high loading of the CB filler in the rubber. Consequently, the existence of the aggregates and the dispersible units, which will be later identified by the scattering method, was not clearly discerned in the TEM image.

III-3. CB in PI Matrix. Next, we discuss the hierarchical structures of the CB filler in the PI rubber matrix. Figure 5 shows the combined USANS, USAXS, and SAXS profiles for the peroxide cross-linked CB/PI(20) where the number "20" designates ϕ_{CB}. The curves shown by the dotted line numbered 1, dashed line numbered 2, and broken line numbered 3 will be discussed later in section IV-1. From the figure we can see the two power-law regions and the Guinier region in between them. However, no upper cutoff length is detected in the observed q range, indicating that the size of the upper cutoff length for the mass-fractal structure is more than the USANS resolution limit of 21 μm ($=2\pi/q_{min}$) and much larger than CB/SBR(20). As will be discussed in detail later, the lower cutoff length (R_{ss}) is also much larger than that for CB/SBR(20) shown in Figure 3, while the exponents (2.3 and 3.4) of the two power-law regions for CB/PI(20) are identical to those of the corresponding power-law regions for CB/SBR(20). This indicates that both mass and surface fractal dimensions remained unchanged with the change of the rubber matrix. It should be noted that no significant difference in the TEM images between CB/SBR(20) and CB/PI(20) could be seen, though the image for CB/PI(20) is not shown here.

III-4. CB in Toluene. An important issue to be clarified here is whether or not the smallest structural unit of the CB filler in the rubber (i.e., the dispersible unit of CB or the lower cutoff objects for the mass-fractal structures) corresponds to the CB aggregate itself. In order to explore this, we dispersed the dry CB powder into toluene under application of a sonic energy. The CB particles with the same loading of the filler (ϕ_{CB} =

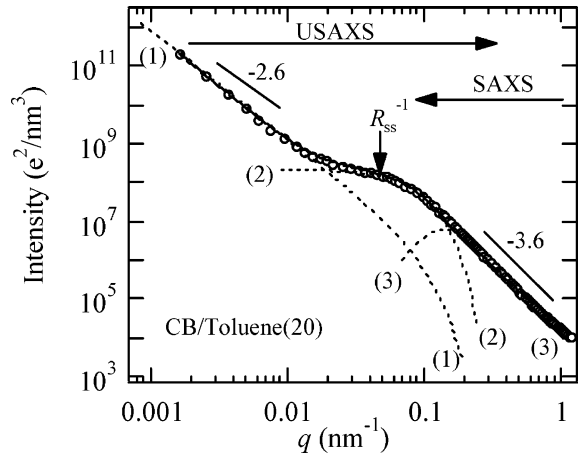

Figure 6. USAXS and SAXS profiles for CB/toluene(20) (symbols). The solid lines and the dotted lines numbered 1 to 3 have the same means as in Figure 5.

20%) were set into a glass capillary tube (diameter = 1 mm) filled in toluene. We used an ultrasonic cleaner for 60 min, and then let them precipitate completely. We carefully irradiated an incident X-ray beam on the precipitates and measured both USAXS and SAXS profiles for the CB/toluene solution (which is hereafter defined as CB/toluene(20)).

The combined USAXS and SAXS data for CB/toluene(20) is shown in Figure 6. The broken curves numbered 1−3 will be discussed later in section IV-1. As will be shown later in conjunction with Figure 9, we can see that the Guinier region for CB/toluene(20) locates at the higher q-region relative to those for the CB-filled rubber compounds. This indicates that the size of the smallest structural unit (i.e., the lower cutoff object) for the mass-fractal structure in the rubbers are larger than that of the fractal object formed in CB/toluene(20) after sonification. In other words, the lower cutoff object in the rubbers is not identical to the smallest structural unit of the CB filler itself. Since the scattering profiles from CB/toluene(20) remained unchanged even after 60 min of sonification, we therefore conclude that the smallest structural unit of CB formed in toluene is the aggregate, i.e., the unbreakable unit of the CB filler. In the rubber matrices, this aggregate further clusters into the higher order structural unit (i.e., the lower cutoff object for the mass fractal structure). We define this lower cutoff object as the dispersible unit in this work. The dispersible unit will be characterized in detail later in section IV-2.

In order to study the surface fractal structure of the pure CB particles, we extended the q range covered by SAXS to that covered by a wide-angle X-ray scattering (WAXS) technique. Figure 7a shows the combined SAXS and WAXS profiles for CB/toluene(20). The WAXS data was shifted vertically in the logarithmic intensity scale to make it match with the SAXS profile with a sufficiently wide overlap q-region as shown in the part (a). From the figure we can see the two peaks indicated by the two arrows on the WAXS profile: a broad amorphous peak at q_a = 15.4 nm^{-1} and a relatively sharp peak at q_c = 17.7 nm^{-1}, which is attributed to a (002) reflection with a Bragg spacing ($d = 2\pi/q_c$) of 3.56 Å. The values of these peaks were determined by the best-fit of the experimental profile with the predicted profile constructed by a weighted average of Lorentzian and Gaussian functions for the broad and sharp components, respectively. Each contribution is shown by the dotted lines numbered 1 and 2 in Figure 7a. It should be noted that the d value determined by WAXS is slightly larger than that for a ideal graphite crystal (d_{002} = 3.35 Å), which is commonly

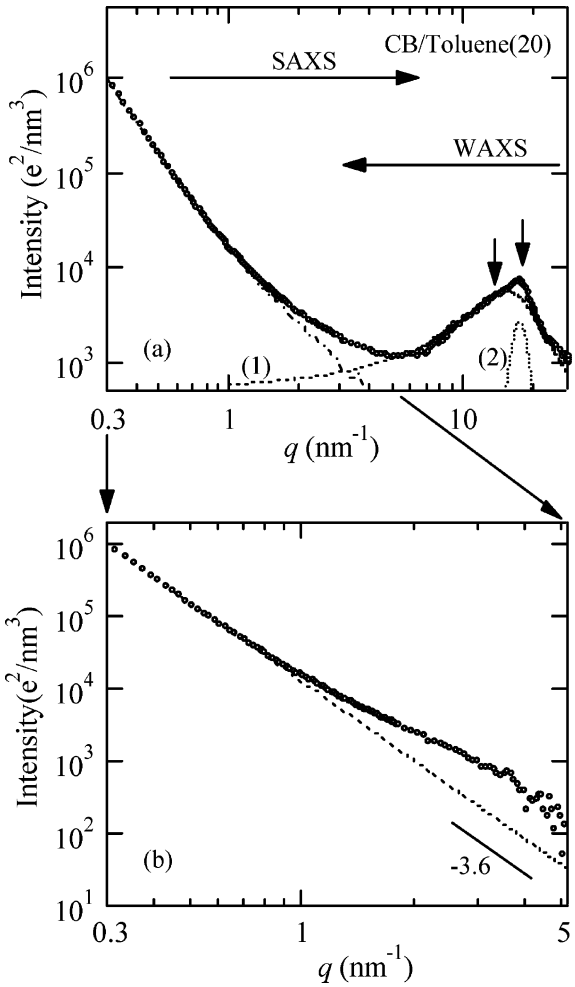

Figure 7. (a) Combined SAXS and WAXS scattering profiles for CB/toluene(20) (symbols). The arrows indicate the peak positions of the two components in CB. The dotted lines numbered 1 and 2, respectively, show the contribution of the broad peak approximated by a Lorentzian and that of the sharp peak approximated by a Gaussian function to the net WAXS profile (dotted lines numbered 1 and 2). The dash-dot line shows the SAXS profile after subtracting the contribution from the WAXS profile. (b) Corrected SAXS profile obtained after subtraction of the amorphous component (symbols).

encountered in CB with an internal inhomogeneous (i.e., turbostratic) structures.[33]

In order to extract the surface fractal dimension of the CB primary particles, we subtracted the contribution of the broad Lorentzian component (curve 1) from the net combined SAXS and WAXS profile. The corrected SAXS profile is shown by the dash−dot line in Figure 7a. Figure 7b shows the corresponding SAXS profile (circular symbols). The power-law with $p = 3.6$ shown by the dotted line is seen at $0.1 < q < 1$ nm^{-1}, the exponent of which is in good agreement with the previous SANS experiments that showed $p = 3.67$ regardless of the CB grades.[32] However, at the higher q range of $q > 1$ nm^{-1}, we can see the deviation from the power-law scattering. We postulate that this excess scattering is due to internal inhomogeneities in the CB particles comprising crystalline and amorphous phases, as will be shown later in part b of Figure 12. Further experiments using a contrast-matching technique in SANS measurements, for which a mixture of deuterated and hydrogenated organic solvents can be used to attain the same scattering contrast as the CB filler, deserve future work in order to study the detailed structure of the internal inhomogeneities.

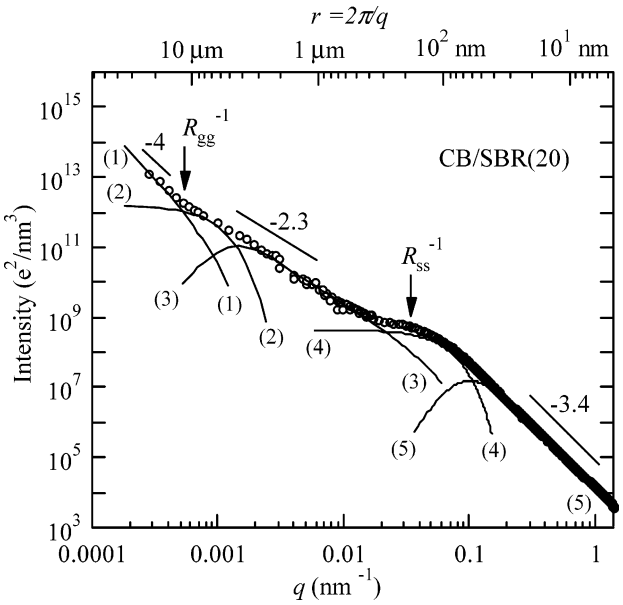

Figure 8. Decomposition of the observed net scattering profile for CB/SBR(20) (symbols) into each scattering component (solid lines) from each structural level comprising the hierarchical structure based on the UF analysis. The solid lines numbered 1 to 5 are the contribution of the first to the fifth term in the rhs of eq 5 to the net theoretical scattering profile.

IV. Analysis of Scattering Curves

IV-1. Quantitative Analysis Based on Unified (UF) Equation: Sizes of Aggregates and Dispersible Units. As mentioned above, the observed SAS scattering profiles contain various information in terms of the multiple levels of the structure elements with the sizes ranging from 1 nm to 21 μm. For example, in the case of CB/SBR(20) shown in Figure 3, the two discrete form-factor profiles (Guinier scattering profiles) and the three discrete power-law scattering profiles with the power exponents of −4, −2.3, and −3.4, respectively, are seen in the profiles in the order of increasing q. In order to analyze the hierarchical structures, the observed net scattering profile should be decomposed into the scattering from each structural element comprising the hierarchical structures. For this purpose, we utilized the unified approach proposed by Beaucage.[26]

We first applied the Beaucage UF equation to the scattering profile for CB/SBR(20) shown in Figure 3. In this case the UF equation is given by eq 5 below

$$I(q) = A\exp(-q^2R_{gg}{}^2/3)q^{-p_1} + B\exp(-q^2R_{gg}{}^2/3) + C\exp(-q^2R_{ss}{}^2/3) \times [\mathrm{erf}(qR_{gg}/\sqrt{6})]^{3D_m}q^{-D_m} + D\exp(-q^2R_{ss}{}^2/3) + E[\mathrm{erf}(qR_{ss}/\sqrt{6})]^{3(2d-D_s)}q^{-(2d-D_s)} \quad (5)$$

On the basis of this approach, the net scattering profile was decomposed into the five profiles shown by the solid lines numbered 1 to 5 in Figure 8. Each profile has the following characteristics. Profile 1, which is given by the first term in the rhs of eq 5, represents the scattering profile given by $I(q) \propto q^{-p_1}$ with $p_1 = 4$ and the lower cutoff length R_{gg} for this power law; the prefactor $\exp(-q^2R_{gg}{}^2/3)$ serves as a damping factor for the power-law at $qR_{gg} > 1$. Profile 2, which is given by the second term in the rhs of eq 5, represents the Guinier scattering from the agglomerate level 2 as a whole having radius of gyration of R_{gg}, as will be shown later in Figure 13f. Profile 3, which is given by the third term in the rhs of eq 5 with $D_m = 2.3$ (mass-fractal dimension), represents the power-law scattering profile $I(q) \propto q^{-D_m}$ with the upper cutoff length of R_{gg} and the

Table 2. Characterizations of CB-Filled Rubber Compounds Used in This Study

code name	polymers	ϕ_{CB}[a]	ω_p (phr)[b]	ω_c (vol %)[c]
CB/SBR(20)	SBR	20	0.8	10
CB/PI(20)	PI	20	1.4	0
CB/PI(20)/UCR[d]	PI	20	0	0
CB/PI(20)/PO[e]	PI	20	1.4	10

[a] Volume fraction of filler particles. [b] Phr (parts per hundred parts of rubber) of peroxide cross-linker. [c] Volume fraction of process oil. [d] Uncross-linked matrix. [e] Cross-linked matrix containing processing oil.

lower cutoff length of R_{ss}; the term $[\mathrm{erf}(qR_{gg}/\sqrt{6})]^{3D_m}$ serves as a damping factor for the power-law at the small q range of $qR_{gg} \leq 1$, while the term $\exp(-q^2R_{ss}^2/3)$ serves as a damping factor for the power-law at $qR_{ss} \geq 1$. Profile 4, which is given by the fourth term in the rhs of eq 5, represents the Guinier scattering profile for the dispersible unit of CB as a whole (agglomerate level 1, as will be shown later in Figure 13e, having a radius of gyration of R_{ss}). Profile 5, which is given by the fifth term of the rhs of eq 5 with $2d\text{-}D_s = 3.4$ (eq 3), represents the power-law scattering profile of $I(q) \propto q^{-(2d-D_s)}$ with the upper cutoff length R_{ss}; the term $[\mathrm{erf}(qR_{ss}/\sqrt{6})]^{3(2d-D_s)}$ serves as a damping factor for the power-law at the small q range at $qR_{ss} \leq 1$.

It is important to note the following points. The power law of $q^{-3.4}$ is observed at $q \geq q_{s,l} \cong 0.2$ nm^{-1}. The value $q_{s,l}$ is greater than R_{ss}^{-1}. Hence the self-similar surface roughness should exist on the surface of the lower cutoff object (the dispersible unit) for the mass-fractal structure, reconfirming the argument previously given in section III-2.

Since no upper cutoff length is seen for the power law scattering of q^{-4} at $q < 3 \times 10^{-4}$ nm^{-1}, only the Guinier scattering function was introduced to describe the lower cutoff length R_{gg} of the power-law on the first term in the rhs of eq 5. The first term arises from a spatial distribution of the agglomerates of level 2, which appears to be homogeneous and to have sharp interfacial boundaries against the rubber matrix at $q < R_{gg}^{-1}$, inside the bulk rubber, as will be described later in Figure 13g.

The solid line in Figure 3 shows the sum of the scattering profiles 1−5 shown in Figure 8. We can confirm that the sum of each scattering profile gives the best-fit to the net observed scattering profiles shown by the open circles. The best-fit yielded the values of R_{gg} and R_{ss} to be 2.0 μm and 29 nm, respectively, with $p_1 = 4.0 \pm 0.05$, $D_m = 2.3 \pm 0.05$, and $D_s = 2.6 \pm 0.05$ (see, Table 3). The proportionality constants ($A-E$) in eq 5 determined from the best-fit are also summarized in Table 3. It is interesting to note that the R_{ss} value, i.e., the radius of gyration of the dispersible unit, is about three times larger than that of the primary CB particles ($R_g = \sqrt{3/5}R_{TEM} \cong 10$ nm). The two arrows in Figure 8 correspond to the q values equal to R_{gg}^{-1} and R_{ss}^{-1}.

We applied the UF approach to the data for CB/PI(20) as well, as shown in Figure 5 with D_m, D_s, and R_{ss} as floating parameters in eq 6 below. In this case no upper cutoff length (R_{gg}) for the mass-fractal structure is observed in the covered q range so that we can set $R_{gg} \rightarrow \infty$ in eq 5. Hence both first and second terms can be neglected and the error function in the third term in the rhs of eq 5 becomes a constant independent of q. Thus, eq 5 is rewritten as

$$I(q) = C\exp(-q^2R_{ss}^2/3)q^{-D_m} + D\exp(-q^2R_{ss}^2/3) + E[\mathrm{erf}(qR_{ss}/\sqrt{6})]^{3(2d-D_s)}q^{-(2d-D_s)} \quad (6)$$

As a result of the best-fit between eq 6 and the data (shown by the symbols), R_{ss}, D_m, and D_s were estimated to be 40 ± 1 nm, 2.30 ± 0.03, and 2.60 ± 0.03, respectively, with the three constants of $C = 7 \times 10^4$, $D = 5.2 \times 10^8$ and $E = 1.7 \times 10^4$ in eq 6. Thus, the R_{ss} value, i.e., the size of the dispersible unit in the PI matrix, was found to be much larger than that for CB/SBR(20), while the dimensions of the mass and surface fractal structures were identical (see Table 3). The solid line in Figure 5 represents the best-fitted profile with the experimental profile based on eq 6. The dotted line numbered 1, the dash-

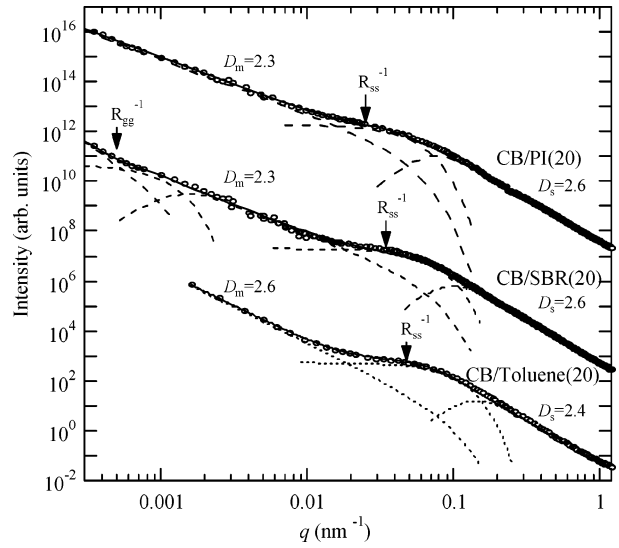

Figure 9. Comparison of the combined SAS profiles for CB/PI(20), CB/SBR(20), and CB/toluene(20) on a common intensity scale and q scale. Each profile was vertically shifted to avoid their overlaps.

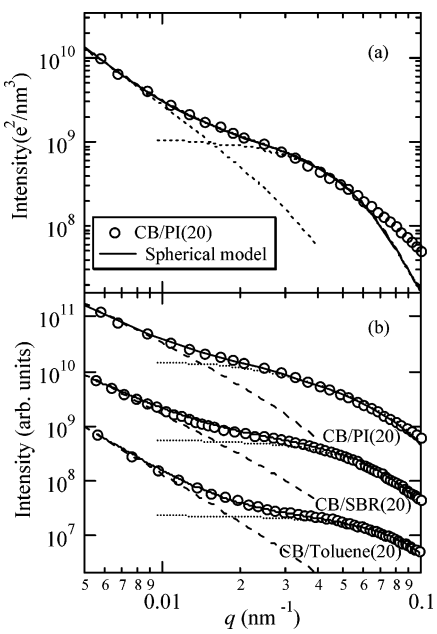

Figure 10. (a) Expanded view of the USAXS scattering profiles for CB/PI(20) in the q range between 0.005 and 0.1 nm^{-1}. The solid line corresponds to the best-fitted theoretical profile using the form factor of the sphere in the modified UF approach with $\bar{R}_d = 34 \pm 6$ nm and $10 < \sigma_R < 15$ nm using eqs 8 to 12. (b) Expanded view of the USAXS scattering profiles for CB/PI(20), CB/SBR(20), and CB/toluene(20). The solid lines correspond to the best-fitted theoretical profiles based on the ellipsoidal models in the modified UF approach by using eqs 11, 13 and 14 with $R_d = 27.4$ nm and $w = 4.0$ for CB/PI(20), $R_d = 27.4$ nm and $w = 1.8$ for CB/SBR(20), and the best-fitted theoretical profile based on the spherical model using eqs 8 to 12 with $R_a = 27.1$ nm and $1 < \sigma_R < 5$ nm for CB/toluene(20), respectively. The broken and dotted lines correspond to the contributions of the first and second term in the rhs of eq 11 to the net theoretical scattering profiles.

Table 3. UF Fitting Results

code name	A^a	B^a	C^a	D^a	E^a	R_{gg} (μm)	R_{ss} (nm)	D_m	D_s
CB/SBR(20)	0.5	1.5×10^{12}	62 000	4.5×10^8	15 000	2.0	29	2.3	2.6
CB/PI(20)			90 000	7×10^8	17 000	>21	40	2.3	2.6
CB/toluene(20)[b]			2300	2.4×10^8	20 000		21	2.6	2.4

[a] Proportionality constant for $I(q)$ in eqs 5 and 6. [b] No USANS measurements.

dotted line numbered 2, and the broken line numbered 3 are, respectively, the contributions of the first, second, and third terms in rhs of eq 6 to the net calculated scattering profiles shown by the solid line in Figure 5.

Figure 6 also displays the best-fit between the experimental profile (open circles) and the theoretical profile (solid line) given by eq 6 for CB/toluene(20). The dotted lines numbered 1, 2, and 3, respectively, display the contributions of the first, second, and third terms in rhs of eq 6 to the net theoretical scattering function $I(q)$. The UF analysis using eq 6 gave us the values of $R_{ss} = 21$ nm $\pm$ 1 nm, $D_m = 2.60 \pm 0.03$, and $D_s = 2.40 \pm 0.03$. These parameters are also tabulated in Table 3. Thus, we can see that the R_{ss} value for CB/toluene(20), i.e., the size of the aggregate, is much smaller than the size of the dispersible unit of the CB-filled elastomers. In other words, the dispersible units consist of a few aggregates. It should be noted that the D_m value for CB/toluene(20) is larger than the D_m value for CB/SBR(20) and CBR/PI(20), implying that the mass-fractal object developed in the toluene solution comprises more densely packed "aggregates" than those developed in the SBR and PI rubbers. We may interpret this difference is primarily attributed to the difference in viscosity of the medium where the diffusion limited aggregation of the aggregates or the "dispersible unit" into the mass fractal objects occurs. Further USANS study to extend the q range showing the corresponding mass-fractal power-law toward a smaller q range deserves future work.

It is also important to note that CB/toluene(20) has a small surface fractal dimension D_s than the cross-linked CB/SBR(20) and CB/PI(20) systems. This implies that the surface of the CB aggregates or the CB primary particle in the rubber matrices is rougher than that in toluene. This may be attributed to the bound rubber phase adhered to the fractal surface of the CB aggregate or the CB primary particle where the phase is expected to have a density much higher than the bulk rubber.

Before leaving this section, we present a comparison of the combined SAS profiles observed for CB/PI(20), CB/SBR(20), and CB/toluene on the same intensity scale and q scale in Figure 9. The three profiles were vertically shifted to avoid an overlap. The figure enables us to recognize the difference of the three systems at a glance in terms of the mass fractal structure developed (R_{gg}, D_m, and R_{ss}) and the surface fractal structure of the CB aggregate or primary CB particle (D_s).

IV-2. Quantitative Analysis Based on Modified UF Equation: Shapes and Sizes of Aggregates and Dispersible Units. From the scattering analysis based on the UF approach, we could quantitatively evaluate the sizes of the aggregates and dispersible units (i.e., the lower cutoff lengths for the mass-fractal structures in air (or toluene) and the rubbers). However, information on their shapes remains unsolved, because the Guinier scattering function is independent of shapes of structures but does depend only on R_g values.[34] Therefore, we attempted to modify the UF analysis by replacing the Guinier's function by a form factor $F(q)$ of the corresponding lower cutoff objects:

$$I(q) \cong A' \exp(-R_{ss}^2 q^2/3) q^{-D_m} + B' F(q) \tag{7}$$

where A' and B' are numerical constants. Note that the form factor should display the Porod law (q^{-4} power law) in the high q-region. However all the scattering profiles showed the deviation from the Porod law at $q > 0.2$ nm^{-1} as is obvious from Figure 9. This deviation is due to the contribution of the scattering from the surface fractal structure of the carbon black (CB) filler to the form factor scattering from the filler particle as a whole. Thus, the data analyses based on eq 7 were performed only at $q < 0.1$ nm^{-1} in order to exclude the contribution from the surface fractal scattering and to selectively analyze shape and size of the particle whose surface roughness is effectively smoothed out. This approximation can be also derived from the treatment proposed by Sinha and coworkers[35] on the cutoff problem for the power-law scattering curves.

Table 4. Fitting Results Based on the Modified UF Analysis

code name	$\overline{R_d}$ (nm)	$\overline{R_a}$ (nm)	w	D_m	D_s[a]
CB/SBR(20)	27		1.8	2.3	2.6
CB/PI(20)	27		4.0	2.3	2.6
CB/PI(20)/UCR	27		3.1	2.3	2.4
CB/PI(20)/PO	27		4.0	2.3	2.6
CB/toluene(20)		27	1.0	2.6	2.4

[a] D_s evaluated by the UF analysis

First, we examined the size and shape of the aggregates found in CB/toluene(20) after sonification, based on an assumption that the shape is spherical with the radius of R_a. Hence, the form factor $F(q)$ is given by

$$F(q) \propto R_a^6 \Phi^2(u) \tag{8}$$

where

$$\Phi(u) = \frac{3}{u^3}(\sin u - u \cos u) \tag{9}$$

with $u = qR_a$. Here we considered the polydispersity of R_a given by a Gaussian function:

$$P(R_a) \sim \exp[(R_a - \overline{R_a})^2/2\sigma_R^2] \tag{10}$$

where $\bar{R}_a$ and σ_R are the average R_a and corresponding standard deviation, respectively. The averaged scattering intensity, $\overline{I(q)}$, is given by

$$\overline{I(q)} \cong A' \exp(-R_{ss}^2 q^2/3) q^{-D_m} + B' \overline{F(q)} \tag{11}$$

with $\overline{F(q)}$ being the average form factor given by

$$\overline{F(q)} = \int_0^\infty P(R_a) R_a^6 \Phi^2(u; R_a)\, dR_a / \int_0^\infty P(R_a)\, dR_a \tag{12}$$

and $R_{ss} = \sqrt{3/5} R_a$. As shown by the solid line in Figure 10(b), eq 11 with $D_m = 2.60 \pm 0.03$, $\bar{R}_a = 27 \pm 3$ nm, and $1 < \sigma_R < 5$ nm could successfully fit the scattering data for CB/toluene-(20) at $q \leq 0.1$ nm^{-1}. We can therefore deduce that the spherical aggregates are formed after sonification of the CB/toluene solution. Note also that D_m obtained here is identical to that estimated with the UF approach, as tabulated in Table 4. It should be noted that Table 4 contains the results of D_s which are obtained by the UF analysis rather than by the modified

UF analysis developed in this section. The information on D_s will be later discussed in section V-2.

Second, following the same treatment using eq 11, we analyzed the form factors of the dispersible units in the rubbers. We fitted the data for CB/PI(20) on the basis of an assumption that the shape of the dispersible unit was again spherical: $F(q)$ and $\overline{F(q)}$ for the dispersible units can be then expressed by eqs 8 and 12, respectively, with a replacement of R_a by the radius of the dispersible unit, R_d. However, as shown in Figure 10a, it was found that the best-fitted scattering profile for the spherical model with $\bar{R}_d = 34 \pm 6$ nm and $10 < \sigma_R < 15$ nm (solid line) by using eq 11 could satisfy only the experimental profile (open circles) up to $q \cong 0.05$ nm^{-1}.

Taking the deviation from the spherical model at $0.05 < q < 0.1$ nm^{-1} into account, we then assumed that the shape of the dispersible unit for CB/PI(20) was ellipsoidal. The scattering intensity from an ellipsoid of revolution having radii of (R_d, R_d, wR_d) with a random orientation is given as follows:

$$F(q) = \int_0^{\pi} (4\pi w R_d^3/3)^2 \Phi^2(u) \sin\beta \, d\beta \qquad (13)$$

where

$$u = qR_d[\sin^2\beta + w^2\cos^2\beta]^{1/2} \qquad (14)$$

and w and β are an aspect ratio of the ellipsoid and a polar angle between the axis of revolution and the reference axis, respectively. In this case, R_{ss} in eq 11 is given by $R_{ss} = R_d[(2 + w^2)/5]^{1/2}$. As shown in Figure 10b, the ellipsoidal model (the solid line calculated by eqs 11 and 13) with $R_d = 27.4 \pm 0.5$ nm and $w = 4.0 \pm 0.2$ shows a good fit to the data (open circles) for CB/PI(20) up to $q = 0.09$ nm^{-1}. The results are also listed in Table 4. It should be noted that consideration of the polydispersity of the radii of the ellipsoidal shape, which is ignored in the above analysis, could improve the small deviation between the observed and calculated profiles in the vicinity of $q = 0.1$ nm^{-1}. It may be also worth noting that the asymptotic scattering behavior of the thin prolate ellipsoid having $w = 4$ is different from that of the thin rod: the latter gives q^{-1} but the former does not.

Third, the modified UF approach was applied to CB/SBR-(20). We confirmed that the spherical model for the dispersible unit with $\bar{R}_d = 34 \pm 6$ nm and $4 < \sigma_R < 10$ nm could only fit the experimental profile up to $q = 0.05$ nm^{-1} (though the fitting result is not shown here). Therefore, as for CB/PI(20), we adopted the ellipsoidal model for the CB dispersible unit in the SBR matrix. As shown in Figure 10b, the ellipsoidal model could fit well the data up to $q = 0.09$ nm^{-1}, and the corresponding R_d and w values were estimated to be $R_d = 27.4 \pm 0.5$ nm and $w = 1.8 \pm 0.3$, respectively (Table 4). Thus, it is clear that the more compact dispersible unit is formed in the SBR matrix, compared to that in the PI matrix even under the same compounding conditions.

We analyzed the effect of the peroxide cross-linking process on the CB dispersible unit in the PI matrix as well. The USAXS scattering profile for CB/PI(20)/UCR, in which PI is not cross-linked (open squares), is plotted in Figure 11 along with the peroxide cross-linked CB/PI(20) (open circles) for a comparison. Note that the data for the cross-linked CB/PI(20) in this figure is the same as the data shown in Figure 10. From the figure we can see the scattering intensity for the system without the cross-linkng process is lower at $q < 0.03$ nm^{-1} than that for the system with the cross-linkng process, while the D_m values are the same for both systems ($D_m = 2.3$). On the basis of the ellipsoidal model shown in the solid line, the best-fit to the data provided $R_d = 27.4$ nm and $w = 3.1$ for the system without the cross-linkng process (Table 4). Thus, the aspect ratio and thereby the overall size of the ellipsoidal dispersible unit were slightly larger when a peroxide cross-linker was incorporated, while the R_d value remained constant. It should be also noted that an effect of the processing oil used for CB/PI(20), which is anticipated to improve dispersion of fillers, on the dispersible units is not significant at all from a comparison of the result between CB/PI(20) and CB/PI(20)/PO (see Table 4).

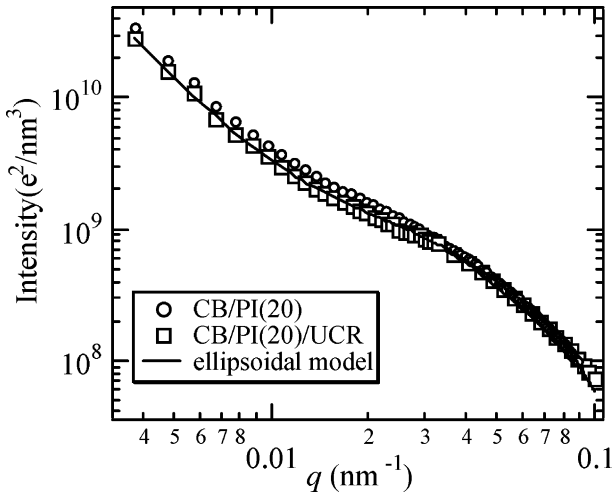

Figure 11. Comparison of the USAXS scattering profiles between CB/PI(20) (circles) and CB/PI(20)/UCR (squares) around the Guinier region. The solid line corresponds to the best-fit to the data for CB/PI(20)/UCR on the basis of the ellipsoidal model by using eqs 11, 13, and 14 with $R_d = 27.4$ nm and $w = 3.1$.

V. Discussion

V-1. Characterization of Aggregate and Hierarchical Structure in CB/Toluene. Figure 12 summarizes the hierarchical structure of the CB filler in toluene based on the scattering results. From the modified UF analysis of the scattering from CB/toluene(20), we found that the CB aggregate had the spherical shape with the average radius of $\bar{R}_a = 27.1 \pm 0.5$ nm, as schematically shown in part d. In fact, this $\bar{R}_a$ value is in good agreement with the average radius calculated from the radius of gyration $R_{ss} = 21$ nm evaluated from the UF analysis ($\sqrt{5/3}R_{ss} = 27$ nm) (see, IV-2 in conjunction with Figure 6). On the basis of the volume consideration, it is reasonable to deduce that the CB aggregate obtained after sonification of the CB/toluene solution is composed of about 9 ($=(\bar{R}_a/R_{TEM})^3$) CB primary particles fused together. In CB/toluene(20), the aggregates further cluster into the mass-fractal agglomerate (shown in part e) with the D_m value of 2.6 via diffusion-limited aggregation of the CB aggregates mediated by attractive interactions between the CB aggregates (Table 3). The aggregates thus correspond to the lower cutoff object for the mass-fractal agglomerate. The primary particle or the aggregate was found to have the self-similar rough surface with $D_s = 2.4$ as schematically illustrated in part a.

Herd et al.[8] studied the morphology of the "aggregates" with the same CB grade (N339) used in this study. It should be noted that the "aggregates" that they defined are not the lower cutoff objects for the mass-fractal objects, but are mass-fractal objects themselves. On the basis of the TEM image discrimination analysis for the CB powder (as manufactured state), they conducted a fine analysis and elucidated that their CB aggregates (our mass-fractal objects) had the upper cutoff length of 103

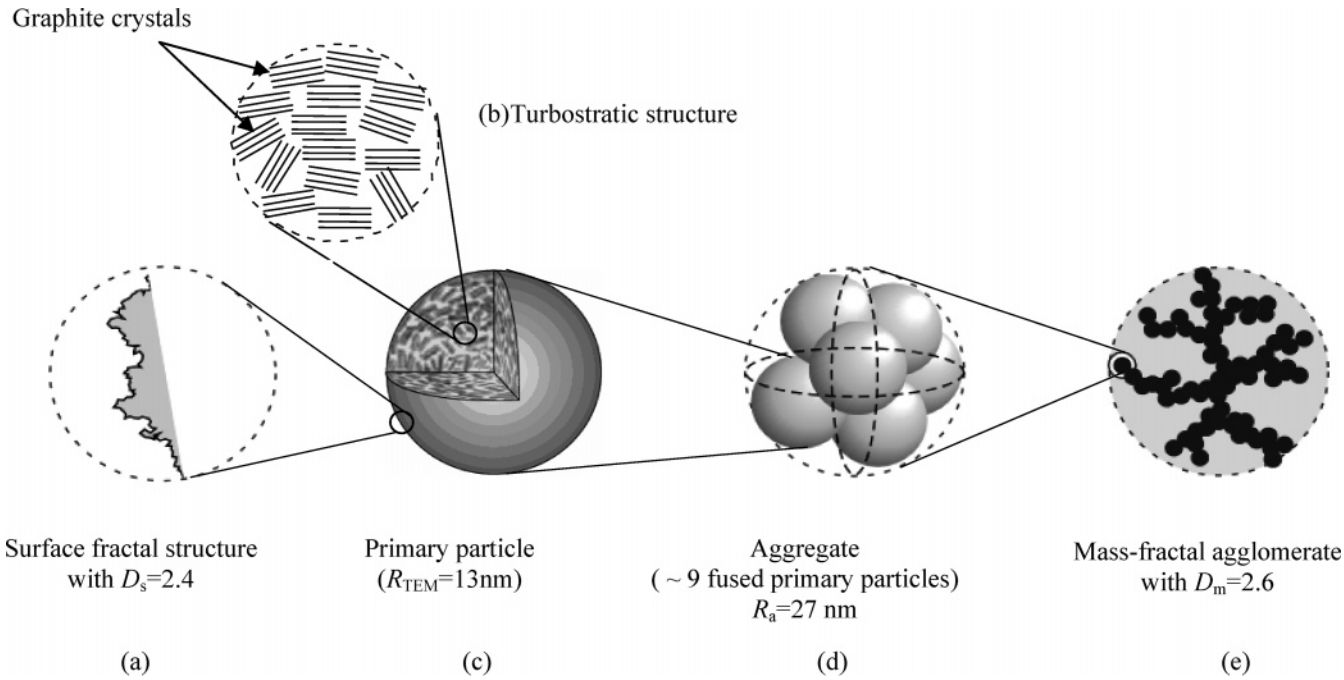

Figure 12. Schematic model for the hierarchical structure of the CB filler in toluene.

nm and the lower cutoff length of 25.8 nm (i.e., the average diameter of the primary CB particles) with the mass-fractal dimension of $D_m = 2.4$. These results are qualitatively in agreement with our results. However on quantitatively bases we found some differences as described below. (i) The lower cutoff length of the mass fractal object is different: $R_{ss} = \sqrt{3/5}R_a = \sqrt{3/5} \times 27 = 21$ nm in our case, while $R_{ss} = \sqrt{3/5} \times 12.9 = 10.0$ nm in their case. They seem to have overlooked the fact that the aggregates defined here in this work, rather than the primary particles themselves, are the lower cutoff object for the mass-fractal structure. It would be difficult to determine by TEM whether the aggregates or primary particles are elementary building blocks for the mass-fractal structure of the CB particles. (ii) According to our experiments, the upper cutoff length of the mass-fractal objects was larger than $2\pi/(2 \times 10^{-3})$ nm $\cong 3$ μm as the power law extends to $q < 2 \times 10^{-3}$ nm^{-1} (see, Figure 6). Hence, the size of our upper cutoff length is at least 1 order of magnitude larger than their TEM results; The smaller upper cutoff length found by them might be attributed to a finite thickness effect of the specimens used for their TEM experiments. (iii) Their power-law exponent is smaller than our value.

One more important thing to be mentioned is that our scattering measurements were conducted in situ in toluene with the high filler concentration, while the TEM method cannot offer such an in situ experiment with high loading of the CB filler. Therefore, we believe that the scattering methods provided a new insight into the morphologies of the aggregates and agglomerates of the CB filler and encourage us to further look into the effect of the rubber matrix on the filler dispersion structures, as will be discussed immediately below.

V-2. Hierarchy of CB Filler in CB/SBR and CB/PI. The CSAS method along with the original UF and modified UF analyses elucidated the hierarchical structure of the CB filler in CB/SBR and CB/PI as summarized in Figure 13. The hierarchical structure is composed of the following structure levels with increasing order of length scale: monomeric units of the polymers (part a); network chains of the elastomers (part b); primary CB particles with surface fractal structure of $D_s =$ 2.6 (part c), which was clarified from Figures 3 and 5 (section IV-1); the aggregates comprising about 9 fused primary CB particles (part d), which was unveiled from Figures 6 and 10 (section IV-2); the agglomerate (level 1) or dispersible unit (part e), which is the smallest building block for the formation of the mass-fractal objects that was also elucidated from Figures 3, 5, and 8 (section IV-1 and Figure 10 (section IV-2)); the agglomerate level 2 or the mass-fractal object built up by the dispersible units (part f); bulk rubber (part g) composed of a dispersion of the mass-fractal objects in the cross-linked bulk rubbers.

It is crucial to note that the hierarchical structure of the CB filler in the rubber matrices is different from that in toluene (Figure 12) in the following point: In CB/toluene, the polymer chains do not exist and thereby the dispersible units composed of the aggregates connected together by the polymer network chains did not exist either. In the case of CB/toluene, the aggregate itself is the smallest building blocks for the formation of the mass-fractal structure.

The morphologies of the dispersible units were found to be an ellipsoid of revolution with $R_d = 27.0 \pm 0.5$ nm and $w = 1.8 \pm 0.2$ for CB/SBR(20), and with $R_d = 27.4 \pm 0.5$ nm and $w = 4.0 \pm 0.2$ for CB/PI(20), respectively. On the basis of the volume consideration, it may be reasonable to conclude that the ellipsoidal dispersible units are composed of about four aggregates on average in PI and about 2 aggregates on average in SBR, respectively. In addition, the larger R_g value and the aspect ratio (w) of the dispersible units in the PI matrix seem to make the upper cutoff length (l_u) of the mass-fractal structure (see Figures 9 and 13) in CB/PI larger than that in CB/SBR, while the D_m values remained unaffected for the two systems.

Yurekli et al.[36] used atomic force microscopy (AFM) to study the CB structures in brominated poly(isobutylene-*ran*-methylstyrene) (BIMS), a synthetic terpolymer of isobutylene, para-methylstyrene, and para-bromomethylstyrene. On the basis of a phase contrast image obtained from tapping mode AFM, they obtained the size distribution of the filler particles measured as a probability distribution of equivalent spherical particle diameter. They found that the dominant particle size at the polymer

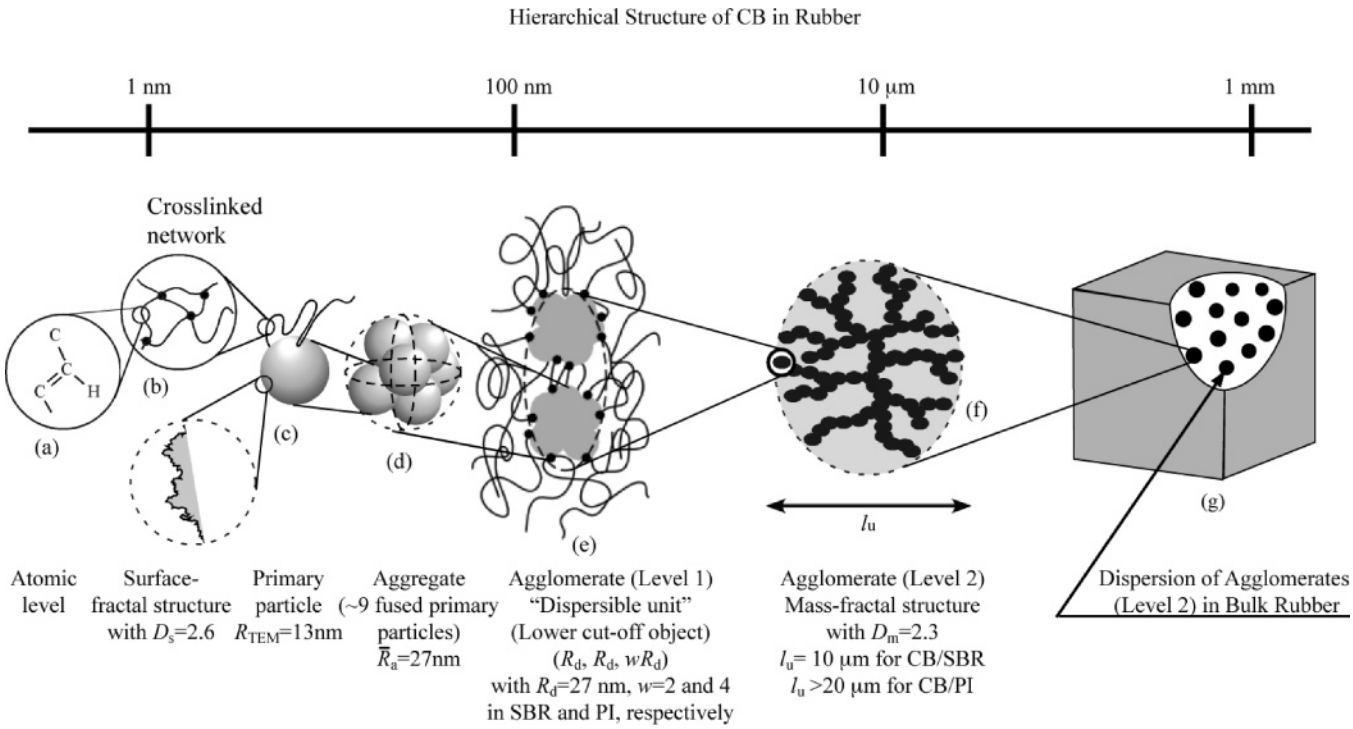

Figure 13. Schematic model for the hierarchical structure of the CB filler in the rubber matrices.

surface was 35 ± 7 nm in diameter, which is slightly larger than that of the primary CB particle (N234 grade, 20 nm in diameter). In addition, they reported that the average aspect ratio (=length/breadth) of the particles was equivalent to about 2 with approximately 90% of the particles having aspect ratios less than 2.5 at the given ϕ_{CB} (=15 and 20%) conditions. Although a quantitative comparison of the dominant structure in the rubber between their AFM and our scattering results is difficult because a two-dimensional projection of the three-dimensional structures is observed with AFM, the size and shape of their dominant CB structure are qualitatively consistent with those of the dispersible units in the rubbers determined by the scattering techniques.

We postulate two reasons for the differences in the size and shape of the ellipsoidal dispersible units in the PI and SBR matrices: One is the difference in the interaction parameters between the CB and the polymers, and the other is the difference in viscosity of the two matrices for the mixing process. In fact, the measured Mooney viscosity of the SBR and PI rubbers was determined to be 54 (ML1+4(100 °C)) and 72 (ML1+4(100 °C)), respectively. This suggests that the PI matrix has higher viscosity and thereby stress level than the SBR matrix. If the viscosity effect is dominant on the dispersible unit, then our results imply that the higher matrix viscosity causes the larger size of the CB dispersible unit (the lower cutoff length). The larger size and aspect ratio may in turn cause the larger mass-fractal objects and thereby the upper cutoff length. In order to further explore the effect of viscosity on the hierarchical structure, further scattering experiments on the structures of the CB filler in the same polymer matrices, but having the different viscosities and different stress levels should be studied. Furthermore, we are currently studying dependence of the mixing time on the hierarchical structures in order to see how and when the dispersible units in the rubbers are formed during the compounding process.

It is also interesting to focus on the surface structure of the CB filler in the different polymer matrices. As shown in Table 4, the D_s values for CB/SBR(20) and CB/PI(20) ($D_s = 2.6$) are larger than that for CB/PI(20)/UCR ($D_s = 2.4$). The value for CB/PI(20)/UCR is in good agreement with that for CB/toluene-(20). The difference in D_s between the cross-linked compounds, CB/PI(20) or CB/SBR(20), and un-cross-linked compound, CB/PI(20)/UCR implies that the cross-linking process affects the surface properties of the CB primary particles or the CB aggregates: The CB surface in the cross-linked rubber is rougher ($D_s = 2.6$) than that in the un-cross-linked rubber or in toluene (bare surface) ($D_s = 2.4$). The table also includes the characteristic parameters for CB/PI(20)/PO, though the scattering data is not included in this paper. The process oil was found not to affect those parameters by comparing the results for CB/PI-(20).

In general, in the case of CB/elastomer systems, three factors are mainly attributed to the deviation from the Porod law in the high q-region, i.e., $I(q) \propto q^{-4}$: one is a surface fractal structure of pure CB particles,[11,31] second is existence of the bound rubber layer at the surface of the CB filler,[37] and third is an internally inhomogeneous (so-called turbostratic) structure of the CB filler.[21] The existence of bound rubber in rubber compounds has been extensively discussed by using various experimental techniques including IR, microcalorimetry, electron spin resonance, and NMR[38−40] and is identified as a rubber phase that cannot be extracted by a good solvent because of the adsorption of rubber molecules on filler surfaces. Since the internal inhomogeneity and the surface fractal structure of the primary CB particles should be identical regardless of the cross-linking process, we postulate that the bound rubber layer adsorbed to the CB filler modifies the surface fractality when the elastomer matrix is cross-linked. If this is the case, the scattering results suggest that the density of the bound rubber layer must be remarkably different from that of the bulk rubber so that the bound layer significantly modifies the electron density profile of the CB surface and thereby the power-law scattering at the corresponding q range. Further study using contrast-matching SANS experiments deserves future works.

VI. Conclusion

By utilizing the USANS, USAXS, and SAXS techniques in concert, we clarified the hierarchical structures of the CB filler in the rubber matrices over a wide range of the reciprocal space as follows:

(i) Possible hierarchical structures of the CB filler highly loaded in the rubber matrices, which are important for practical applications, were in situ elucidated for the first time over the wide length scales ranging from 1 nm to 21 μm.

(ii) The CB filler used in this study formed the spherical aggregates with the average radius $\bar{R}_a = 27$ nm and the size distribution characterized by $1 < \sigma_R < 5$ nm, which is the unbreakable structural unit of the CB filler resulted after sonification in toluene: the aggregate is composed of about the nine primary CB particles fused together.

(iii) The aggregates further formed the higher order mass-fractal agglomerate with $D_m = 2.6$ in toluene (Figure 12). The surface fractal dimension D_s of the CB filler in toluene was estimated to be 2.4, which was in good agreement with the previous SANS data.[32]

(iv) In the SBR matrix, the CB aggregates were found for the first time to further cluster into the higher order structure defined as the dispersible unit, i.e., the smallest structural element (or the lower cutoff object) which builds up the higher order mass-fractal structures. The shape of the dispersible unit was well approximated by the ellipsoid of revolution with $R_d = 27$ nm and $w = 1.8$, respectively. On the basis of the volume consideration, it was found that the dispersible unit was composed of the two aggregates on average connected together by the rubber networks. The mass-fractal and surface-fractal dimensions were estimated to be $D_m = 2.3$ and $D_s = 2.6$, respectively. The mass-fractal objects having the upper cutoff length l_u of 10 μm were dispersed in the bulk cross-linked SBR rubber matrix (Figure 13).

(v) In the PI matrix, the shape of the dispersible unit of the CB filler was also approximated by the ellipsoid of revolution with $R_d = 27$ nm and $w = 4.0$. On the basis of the volume consideration, the dispersible unit was found to consist of the four aggregates on average bound together by the PI chains more or less linearly by the rubber networks, indicating that the prolate ellipsoidal shape in PI was more extended than that in SBR. The enlarged size of the dispersible units was found to enlarge the upper cutoff length of the mass-fractal structures as well ($l_u > 20$ μm), though the mass-fractal dimensions themselves remained unchanged (Figure 13). The difference in the size and shape of the ellipsoidal dispersible units could be due to the difference in attractive interactions between the CB and the polymers (PI or SBR) and/or the difference in viscosity and thereby a stress level built up in the two matrices during the compounding process. Furthermore, we found that the size of the ellipsoidal dispersible unit was slightly enlarged after the cross-linking process, while the effect of the processing oil on the dispersible units was not significant (Table 4).

Acknowledgment. We thank Dr. Y. Ishikawa, The Yokohama Rubber Co., Ltd., for providing invaluable comments and all the samples used in this study.

References and Notes

(1) Koenig, J. L. *Acc. Chem. Res.* **1999**, *32*, 1.
(2) Eggers, H.; Schummer, P. *Rubber Chem. Technol.* **1996**, *69*, 253.
(3) Donnet, J. B.; Bansal, R. C.; Wang, M. J. *Carbon Black: Science and Technology*; Marcel Dekker Inc.: New York, Basel, Hong Kong, 1993.
(4) Medalia, A. I. *J. Colliod Interface Sci.* **1967**, *24*, 393.
(5) Medalia, A. I.; Heckman, F. A. *Carbon* **1969**, *7*, 567.
(6) Hess, W. M.; Ban, L. L.; McDonald, G. C. *Rubber Chem. Technol.* **1969**, *42*, 1209.
(7) Hess, W. M.; McDonald, G. C.; Urban, E. M. *Rubber Chem. Technol.* **1972**, *44*, 204.
(8) Herd, C. R.; McDonald, G. C.; Hess, W. M. *Rubber Chem. Technol.* **1992**, *65*, 107.
(9) Ikeda, Y.; Katoh, A.; Shimanuki, J.; Kohjiya, S. *Macromol. Rapid Commun.* **2004**, *25*, 1186.
(10) Schaefer, D. W.; Agamalian, M. *Curr. Opin. Solid State Mater. Sci.* **2004**, *8*, 39.
(11) Rieker, T. P.; Hindermann-Bischoff, M.; Ehrburger-Dolle, F. *Langmuir* **2000**, *16*, 5588.
(12) Rieker, T. P.; Misono, S.; Ehrburger-Dolle, F. *Langmuir* **1999**, *15*, 914.
(13) Ehrburger-Dolle, F.; Hindermann-Bischoff, M.; Livet, F.; Bley, F.; Rochas, C.; Geissler, E. *Langmuir* **2001**, *17*, 329.
(14) Hoinkis, E.; Lima, E. B. F.; Schubert-Bischoff, P. *Langmuir* **2002**, *20*, 8823.
(15) Petrovic, Z. S.; Cho, Y. J.; Javni, I. *Polymer* **2004**, *45*, 4285.
(16) Rajan, G. S.; Sur, G. S.; Mark, J. E. *J. Polym. Sci., Part B: Polym. Phys.* **2003**, *41*, 1897.
(17) Suryawanshi, C. N.; Pakdel, P.; Schaefer, D. W. *J. Appl. Crystallogr.* **2003**, *36*, 573.
(18) Vu, B. T. N.; Mark, J. E.; Schaefer, D. W. *Composite Interfaces* **2003**, *10*, 451.
(19) Zhang, Y.; Ge, S.; Tang, B.; Koga, T.; Rafailovich, M. H.; Sokolov, J. C.; Peiffer, D. G.; Li, Z.; Dias, A. J.; McElrath, K. O.; Lin, M. Y.; Satiga, S. K.; Urguhart, S. G.; Ade, H.; Nguyen, D. *Macromolecules* **2001**, *34*, 7056.
(20) Lo Celso, F.; Triolo, A.; Negroni, F.; Baron, M. P. S.; Rauch, H.; Triolo, R. *Appl. Phys. A: Mater. Sci. Process.* **2002**, *74*, S1430.
(21) Schaefer, D. W.; Rieker, T.; Agamalian, M.; Lin, J. S.; Fischer, D.; Sukunaran, S.; Chen, C.; Beaucage, G.; Herd, C.; Ivie, J. *J. Appl. Crystallogr.* **2000**, *33*, 587.
(22) Schaefer, D. W.; Suryawanshi, C.; Pakdel, P.; Ilabsky, J.; Jemian, P. R. *Physica A* **2002**, *314*, 686.
(23) Bonse, U.; Hart, M. *Appl. Phys. Lett.* **1965**, *7*, 238.
(24) Aizawa, K.; Tomimitsu, H. *Physica B* **1995**, *213−214*, 884.
(25) Koga, T.; Hart, M.; Hashimoto, T. *J. Appl. Crystallogr.* **1996**, *29*, 318.
(26) Beaucage, G. *J. Appl. Crystallogr.* **1995**, *28*, 717.
(27) Hart, M.; Koga, T.; Takano, Y. *J. Appl. Crystallogr.* **1995**, *28*, 568.
(28) Rathie, J.; Ruland, W. *Colloid Polym. Sci.* **1976**, *254*, 358.
(29) Hendricks, R. W. *J. Appl. Crystallogr.* **1972**, *5*, 315.
(30) Hashimoto, T.; Tanaka, H.; Koizumi, S.; Naka, K.; Chujo, Y. *J. Appl. Crystallogr.*. **2007**, *40*, s73.
(31) Schmidt, P. W. *J. Appl. Crystallogr.* **1991**, *24*, 414.
(32) Gerspacher, M.; O'Farrell, C. P. *Elastomerics* **1991**, 35.
(33) Speck, J. S.; Endo, M.; Dresselhaus, M. S. *J. Cryst. Growth* **1989**, *94*, 834.
(34) Guinier, A.; Fournet, G. *Small-Angle Scattering of X Rays*; Wiley: London, 1955.
(35) Freltoft, T.; Kjems, J.; Sinha, S. K. *Phys. Rev. B* **1986**, *33*, 269.
(36) Yurekli, K.; Krishnamoorti, R.; Tse, M. F.; McElrath, K. O.; Tsou, A. H.; Wang, H.-C. *J. Polym. Sci., Part B: Polym. Phys.* **2001**, *39*, 256.
(37) Gessler, A. M. *Rubber Age* **1969**, *101*, 54.
(38) Fielding, J. H. *Ind. Eng. Chem.* **1937**, *29*, 880.
(39) Waston, W. F. *Ind. Eng. Chem.* **1955**, *47*, 1281.
(40) Stikney, P. G.; Faub, R. D. *Rubber Chem. Technol.* **1964**, *37*, 1299.

MA071867L